Friction and fracture characteristics of engineered crumb-rubber concrete at microscopic lengthscale

Akono, Ange-Therese; Chen, Jinxin; Kaewunruen, Sakdirat

DOI:
10.1016/j.conbuildmat.2018.04.141

Document Version
Peer reviewed version

Citation for published version (Harvard):
Akono, A-T, Chen, J & Kaewunruen, S 2018, 'Friction and fracture characteristics of engineered crumb-rubber concrete at microscopic lengthscale', *Construction and Building Materials*, vol. 175, pp. 735-745. https://doi.org/10.1016/j.conbuildmat.2018.04.141

Friction and Fracture Characteristics of Engineered Crumb-Rubber Concrete at Microscopic Lengthscale

Ange-Therese Akono[a,b,c,*], Jiaxin Chen[c], Sakdirat Kaewunruen[d,e]

[a]*Department of Civil and Environmental Engineering, Northwestern University, 60208, USA*
[b]*Department of Mechanical Science and Engineering, University of Illinois at Urbana-Champaign, 61801, USA*
[c]*Department of Civil and Environmental Engineering, University of Illinois at Urbana-Champaign, 61801, USA*
[d]*Department of Civil Engineering, School of Engineering, University of Birmingham, Birmingham B15 2TT, United Kingdom*
[e]*Birmingham Centre for Railway Research and Education, School of Engineering, University of Birmingham, Birmingham B15 2TT, United Kingdom*

Abstract

Using small-scale depth-sensing techniques, we shed light on the determinants of friction and hardness in engineered crumb rubber-reinforced concrete with applications into railway sleeper ties. Microscopic scratch tests were carried out to assess the hardness, friction and fracture behavior of concrete specimens reinforced with crumb rubber inclusions. Optical microscopy and scanning electron microscopy are utilized to identify the micro-constituents. The partial replacement of aggregates with crumb rubber particle leads to an increase in the friction coefficient and the fracture toughness and a slight decrease in strength properties. Our research suggests that the crumb rubber particle specific area may play a role in dictating the levels of enhancement in friction coefficient. In addition, improper bonding at the cement/rubber interface is shown to result in poor strength characteristics. Furthermore, crumb rubber particles contribute to a higher durability as evidenced by sustained high values of the friction coefficient even in presence of surface lubrication with water or oil. Overall our study highlights the beneficial role of crumb rubber on the friction and fracture behavior while emphasizing the need for more research into the effect of specific surface area and interface bonding.

Keywords: crumb-rubber concrete, Scratch tests, Hardness, Friction, Fracture Toughness

1. Introduction

Crumb rubber concrete is an alternative way to reuse rubber waste and prevent pollution of the environment [1]. Up to 12 million tons of rubber waste are disposed annually in both the US and Europe [2, 3]. Recycling rubber into advanced construction materials provides a way to alleviate the pressure to landfills. A byproduct of the petroleum engineering industry, tire wastes are estimated at 75 million tons per year in the United States alone [4]. Tire wastes are problematic because (i) they are non-biodegradable, (ii) they require a significant amount of space, (iii) they pose a fire hazard [5], and (iv) they serve as a breeding ground for mosquitoes and larvae. A highly-explored strategy to recycle waste tire consists in embedding crumb rubber in cement mixtures for structural applications such as railway concrete sleepers [6, 7], asphalt pavements [8], or precast concrete [9].

Although previous studies have focused on the strength characteristics of rubber-reinforced concrete [5, 10], the friction characteristics have received little attention. For instance, Liu *et al.* recorded the mechanical and durability properties of the crumb rubber concrete from the macro level [2]. A negative correlation was observed between the compressive strength and the rubber content [11]. Taha *et al.* investigated the mechani-

*Corresponding author
Email address: ange-therese.akono@northwestern.edu (Ange-Therese Akono)

cal and fracture properties of rubber concrete using quasibrittle fracture mechanics models. They concluded to the existence of an optimal replacement ratio for tire rubber particles to enhance fracture toughness without compromising strength [12]. Ganesan *et al.* studied the flexural fatigue behavior of self-compacting shredded rubber concrete and showed that a 15 percentage or 20 volume percentage replacement of rubber would significantly improve the distribution of the fatigue life. [13]. Ganesan *et al.* studied the strength and durability characteristics of self-compacting rubberized concrete with or without steel fibers. They found that the addition of steel fibers can compensate the loss of strength due to by rubber addition [14]. Nevertheless, in the aforementioned studies, the rheological behavior was not considered. The impact of tire particle/cement matrix bonding was not studied. Finally, the effect of surface treatment on the mechanical performance was not investigated. As friction and wear are important measures of the durability of railway tracks, new studies are needed. To this end, we rely on micro-rheology tests such as scratch testing to gain a fundamental understanding at the micro- and meso-scale.

In order to understand the friction and fracture response, we rely on scratch testing. Other methods such as atomic force microscopy (AFM) [15] and lateral force microscopy (LFM) [16] have been suggested in the past to measure the friction. However, the AFM/LFM techniques present several drawbacks such as tedious force calibration procedure, and unknown probe tip which makes it challenging to gather valuable quantitative information regarding the friction and fracture behavior. Another challenge is the resolution which remains at the nanoscale. In practice, AFM/LFM methods have been used to yield qualitative data regarding the topography and morphology of cementitious materials. For instance, atomic force microscopy (AFM) and lateral force microscopy (LFM) techniques have been employed to investigate the nanostructure and microstructure of cement hydration products [17, 18, 19]. Herein, we select constant-load and progressive-load scratch testing for its accuracy, reliability and rigor.

Scratch tests consist in pushing a sharp diamond probe across the surface of a weaker material. Scratch tests are frequently used to characterize the friction behavior of metals, polymers, thin films, coatings, and ceramics [20, 21, 22, 23, 24]. Very recently, scratch tests have been applied to characterize the tribology of cementitious materials and geomaterials, which exhibit a large degree of heterogeneity [25]. To our knowledge, scratch tests have not yet been applied to crumb rubber-reinforced concrete. A major challenge is the large range of scale between the whole concrete at the meso and macroscopic scale and the micro-constituents at the microscale. Herein, we apply fracture analysis, strength and hardness relationships, and friction analysis to scratch testing in order to understand the tribological behavior of crumb-rubber concrete at different length-scales and under different loading conditions and surface treatment options.

2. Materials and Methods

Four different types of crumb-rubber reinforced concrete were synthesized at the Birmingham Centre for Railway Research and Education at the University of Birmingham. The mix design is summarized in Table. 1. Mix 1 is the control material, which consists of cement, water, fine aggregate, and coarse aggregate. Table 2 provides the gradation of the aggregates used in this study. In order to compensate for the potential loss in mechanical resistance due to the addition of crumb-rubber particles, fume silica was introduced in Mix 2–4 at a reason of 10% in weght with respect to the mass of fine aggregates. Mix 2 was reinforced with silica fume whereas both Mix 3 and Mix 4 were reinforced with rubber with a mass fraction of respectively 5% and 10% with respect to the mass of fine

Material	Cement (kg)	Water (kg)	Fine Aggregate (kg)	Coarse Aggregate (kg)	Silica fume (kg)	Rubber (kg)
Mix 1	530	233	630	986	0	0
Mix 2	477	233	630	986	53	0
Mix 3	477	233	599	986	53	32
Mix 4	477	233	567	986	53	63

Table 1: Design of crumb-rubber reinforced concrete systems considered in this study.

Serial no.	Sieves (mm)	% retained	Cumulative % retained	% fine
1	20	0	0	100
2	16	0	0	100
3	10	21	21	79
4	6.7	67.5	88.5	11.5
5	4.75	9	97.5	2.5
6	Base	2.5	100	0

Table 2: Aggregate Gradation Table

Properties	Specification	Unit
SiO_2	>90	%
Retention on 45 μm sieve	<1.5	%
H_2O (when packed)	<1.0	%
Bulk Density (U)	200 – 350	kg/m^3
Bulk Density (D)	500 – 700	kg/m^3

Table 3: Chemical and Physical Properties of Silica Fume

aggregates. Silica fume, grade 940 was utilized for Mix 2–4 with the chemical and physical properties of silica fume given in Table-3. Two different sizes of crumb rubber were used: 425 μm with a specific gravity of 1.14 ±0.02 for Mix 3, and 75 μm with a specific gravity of 1.14±0.03 for Mix 4. For each design, 5.5-in.×2-in.×1-in. specimen blocks were manufactured. The specimens were subsequently aged for 28 days prior to microscopic examination and testing.

2.1. Material Preparation

In order to ensure accurate measurements, a rigorous specimen preparation procedure was devised so as to yield a low surface roughness relative to the maximum penetration depth [26]. The specimens were machined using a top-table bandsaw and later embedded under vacuum in an epoxy resin. A linear-precision diamond saw was later utilized to yield 5-mm thick cylindrical specimens with rigorously flat top and bottom faces.The resulting specimens were mounted onto metal disks using cyano-acrylate adhesive. The mounted specimens were then ground and polished using a semi-automatic grinder/polisher. Grinding occurred using silicon carbide abrasive discs of different gradations, consecutively 240, 400, 600, 800, and 1200. Afterward, polishing took place using colloidal suspensions of polycrystalline diamond with particle size consecutively 3 μm, and 1 μm. In between each steps of the grinding and polishing phases, the specimens were rinsed in N-Decane using an ultrasonic bath. The quality of the polished

surface was assessed via optical microscopy and surface profilometry. After grinding and polishing, the specimens were stored in a vacuum desiccator at room temperature to prevent water-induced degradation[27].

2.2. Micro-structural Characterization

Scanning electron microscope (SEM) was used to image the polished crumb-rubber cement specimens. A JEOL JSM-6060LV Low Vacuum Scanning Electron Microscope (SEM) was utilized at the Frederick Seitz Materials research Laboratory with an accelerating voltage of 15–20 kV and a working distance of 10 mm. Fig.1 displays representative SEM images for Mix 3. A matrix-inclusion micro-structure is observed. The matrix phase is hardened cement whereas the inclusions consist of aggregates and rubber particles. The aggregate particles (light grey) are 200–2000 μm in size. In particular, imperfect bonding is observed between the rubber particles and the surrounding hardened cement matrix.

2.3. Scratch Testing

Constant load scratch tests were applied to characterize the hardness and friction properties. All tests were conducted using a Micro Scratch Testing equipment (MST), that was compliant with the standards ASTM G171, ASTM D7187, and ASTM D7072 [28, 29]. The equipment featured a load resolution of 0.01 mN and a depth resolution of 0.05 nm. The scratch testing unit was integrated with a high-resolution video microscope to allow the precise positioning of the test. As shown in Fig. 2, in our experiments, a sphero-conical diamond stylus was pushed across the surface of the material while applying a constant or linearly increasing vertical force. In all tests, a Rockwell C probe was used, characterized by a tip radius $R = 200\ \mu$m and a half-apex angle $\theta = 60\ ^\circ$. The scratch probe was accurately measured using scanning confocal microscopy. Prior to testing, the specimen surface profile was measured via a surface scan using a contact load of 3 mN. During the test, continuous stiffness measurement was utilized to record the forces and the penetration depth in real time along the scratch path. At the end of each test, a panorama image of the residual top surface was captured. In this study, the temperature was held constant at $72 \pm 2\ ^\circ$F, the testing took place under an acoustic enclosure, and the scratch probe was thoroughly cleaned prior to each tests to prevent debris accumulation.

Table 4 displays the scratch parameters used in this study. A total of 304 scratch tests were performed following eight different protocols. We carried out both meso-scale tests, with a constant load of 15 N, and microscale tests, with a constant load of 1 N. In addition, for progressive-load testing, the vertical force was linearly increased from 0.1 N to 2 N. The meso-scale tests were carried out to assess the effective behavior of each mix (Protocol P1) as well as the influence of surface treatment (protocols P2 and P3). Fracture scratch tests (protocol P4) were performed to evaluate the fracture toughness of each mix design. For protocols P1–P4, the location was selected randomly within a given material specimen, Mix 1–4. In contrast, for protocols P5–P9, in-situ optical microscopy was utilized to select an aggregate, silica, rubber particle or a cement matrix space. Microscale scratch tests (protocols P5 and P6) were performed to measure the contribution of each micro-constituent— aggregate, micro-silica, cement paste, and rubber—to the overall behavior. Finally, we investigated the effect of loading rate and scratching speed on the measured scratch hardness and friction coefficient (protocols P7–9).

3. Theory

3.1. Friction and Hardness

Table 4 defines the mathematical notations employed in this study. The friction and hardness were analyzed following

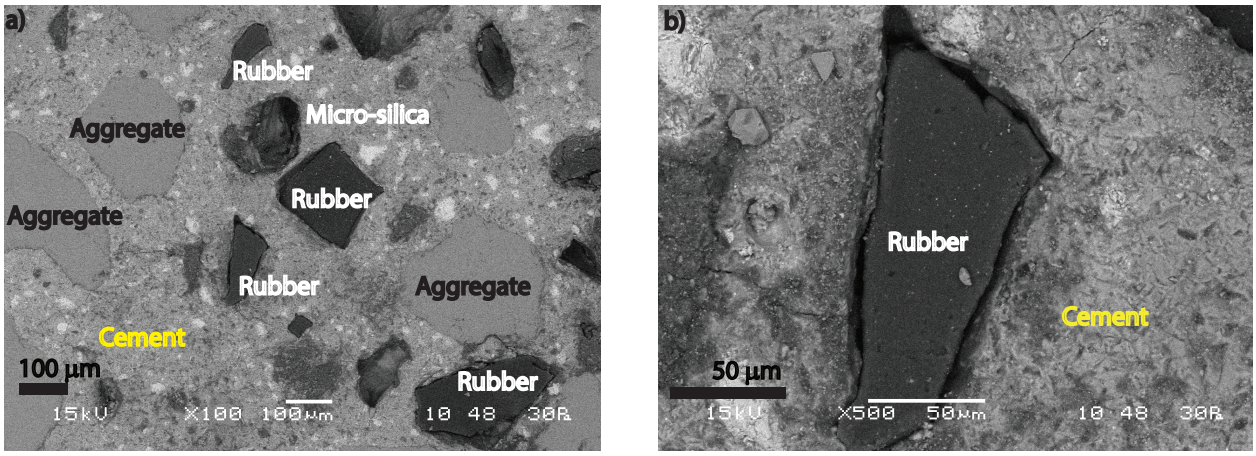

Figure 1: a) Scanning Electron Microscope images of crumb-rubber concrete cement Mix 4 to identify the micro-constituents. The particle identified are aggregate and silica fume inclusions, in light grey, and rubber, in black.

Protocol	P	V	X	Surface Lubricant	System
P1	15	6.0	3	None	Mix 1–4
P2	15	6.0	3	Deionized Water	Mix 1–4
P3	15	6.0	3	Oil	Mix 1–4
P4	0.1–2.0	6.0	3	None	Mix 1 –4
P5	1	0.2	0.1	None	Rubb.
P6	1	2.4	0.2	None	Agg., Cem., Sil.
P7	0.1	2.4	0.2	None	Agg.
P8	1	0.4	0.2	None	Agg.
P9	0.1	0.4	0.2	None	Agg.

Table 4: Scratch protocols for our study. A total of 304 scratch tests was carried out. P is the prescribed vertical load in N. V is the scratch speed in mm/min, X is the scratch length in mm. Agg. = aggregate. Cem. = cement paste. Sil. = silica.

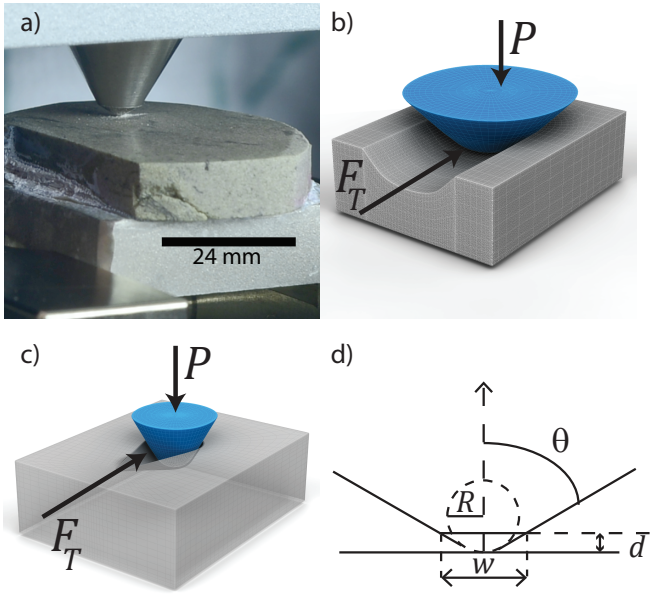

Figure 2: a) Digital photograph of a scratch test. Credits: Ange-Therese Akono, Pooyan Kabir, UIUC, 2016. b) Constant-load scratch test. c) Progressive-load scratch test. d) Scratch probe geometry. d is the penetration depth, F_T is the horizontal force, and P is the vertical force. R is the probe tip radius, meanwhile θ is the half-apex angle and w is the scratch width.

Mathematical symbol	Physical meaning
A	horizontally-projected load-bearing contact area
β	Weibull shape parameter
d	Penetration depth
$\Delta\phi$	Increase in porosity due to improper bonding
d_t	scratch probe transition depth
F_T	Scratch horizontal load
H	Hardness
l_r	rubber inter-particle distance
K_c	Fracture toughness
μ	Apparent friction coefficient
η	Weibull scale parameter
P	Scratch vertical load
p	perimeter
R	Probe tip radius
r	size of rubber particles
t	thickness of rubber particles
θ	Half-apex angle of probe
V	Scratch speed
w	Scratch width
X	Scratch path
ϕ_r	volume content rubber

Table 5: Description of the mathematical symbols used in this study.

ASTM G171-03 [29]. In turn, the scratch hardness provides information regarding the material strength characteristics [30]. The scratch hardness was computed as the ratio of the applied constant vertical force P to the vertically projected contact area:

$$H = \frac{P}{\frac{\pi}{8} w^2} \tag{1}$$

In this study, the vertically projected area, $\pi/8w^2$ is calculated from the scratch width. In turn, the scratch width w is calculated from the measured penetration depth as:

$$w = \begin{cases} 2\sqrt{R^2 - (R-d)^2} & d \le d_t \\ 2\left(d - R(1-\sin\theta)\right)\tan\theta + 2R\cos\theta & d \ge d_t \end{cases} \tag{2}$$

Herein d is the penetration depth that is recorded in real time using high-accuracy sensors, R is the probe tip radius, and θ is the probe half-apex angle. In particular, $d_t = R(1-\sin\theta)$ is the scratch probe transition depth from the spherical into the conical domain. Analogously, the friction coefficient μ is defined as the ratio of the horizontal force F_T to the vertical force P:

$$\mu = \frac{F_T}{P} \tag{3}$$

3.2. Fracture Analysis

Nonlinear fracture mechanics was employed to relate the horizontal force F_T to the fracture toughness K_c [31, 32, 33]:

$$K_c = \frac{F_T}{\sqrt{2pA}} \tag{4}$$

Where, $2pA$ is the probe shape function that depends on the geometry of the scratch probe as well as the penetration depth d [32, 31]. In our tests, the function $2pA(d)$ was calibrated using a reference materials as described in [32]. d is the penetration depth, which is measured using high-accuracy sensors. The theoretical model is derived in details in [31, 32, 33] using the J-integral, the energetic size effect law, and computational fracture mechanics. In particular, the method was validated on polymers, ceramics, and metals [31] and has been applied to characterize the fracture behavior of a wide range of materials including but not limited to cement-polymer composites [34], rocks and cement paste [35], and organic-rich shale [36]. Herein, we apply the scratch fracture method to understand the influence of crumb rubber reinforcement on the fracture behavior.

4. Results

4.1. Individual Test Results

Fig. 3 illustrates the analysis procedure from individual constant-load and progressive-load scratch tests. For instance, consider a single scratch test carried out under a constant vertical load of 15 N. Given the continuous stiffness measurement system, the forces—horizontal F_T, and vertical P—as well as the depth d are recorded every 3 μm. Fig. 3 a) displays the continuous evolution of the force and depth profiles along the scratch path X. The depth profile d yields the width profile using Eq. (2). In turn, the width can be utilized to compute the hardness along the scratch path using Eq. (1). The force measurements can also be used to compute the friction coefficient μ as shown. Due to the heterogeneity of the specimen— consisting of hardened cement paste, aggregates, silica fume, and crumb rubber—, large variations occur along the scratch path for both the hardness and the friction. In particular, the maximum penetration depth oscillates between 52 μm and 95 μm; the hardness varies between 0.20 and 0.47 GPa, and the the friction coefficient varies between 0.06 and 0.56. Thus, each individual constant-load test yields 1,000 independent measurements of the friction coefficient μ and of the scratch hardness H.

Similarly, Fig. 3 b) displays the force and depth measurements recorded during a progressive-load test with a maximum vertical force of 2 N. In turn, the penetration depth increases up

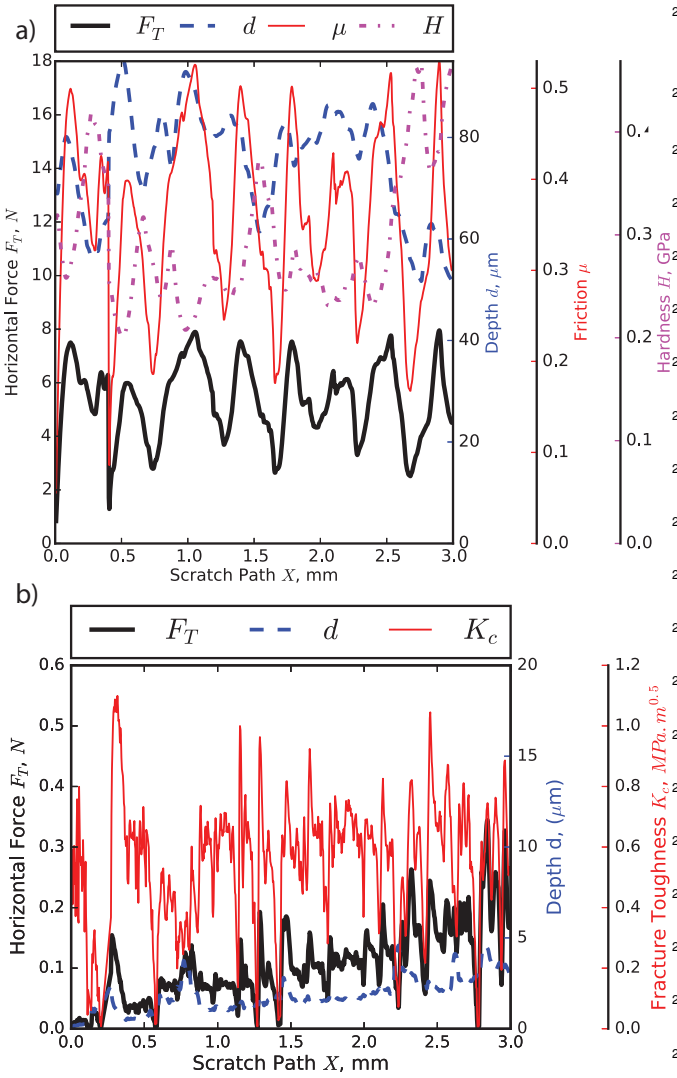

Figure 3: a) Friction and hardness analysis from a single constant-load tests with a constant vertical force equal to 15 N. b) Fracture toughness analysis from a progressive-load individual test with a maximum vertical force of 2 N. Tests on crumb-rubber Mix 3.

to 4.6 μm. By application of Eq. (4), the fracture toughness can be estimated along the scratch path: K_c oscillates around a mean value of 0.55 MPa $\sqrt{m}$ with a standard deviation of 0.2 MPa $\sqrt{m}$. Thus,each individual progressive-load test yields 1,000 independent measurements of the fracture toughness K_c.

4.2. *Effect of Scratch Speed and Normal Load*

From a method development perspective, it is important to understand the influence of the prescribed normal load and scratch speed on the measured friction coefficient. Similarly, from an application standpoint, different train loads and speed will result in different rates and levels of mechanical loads applied locally. Thus we carried out a set of constant-load scratch tests on the aggregate phase at two different speeds, 400 mm/min and 2400 mm/min, and two different load levels: 0.1 N, and 1 N, following protocols P 6–9 in Table 5. For simplicity, we focused on a single micro-phase: aggregate. Fig. 4 the frequency distribution of the scratch friction coefficient μ and of the scratch hardness H for both load levels and scratch speeds.

On the one hand, the scratch load alters the shape of the frequency distribution and the median value of the friction coefficient. In particular, a very small increase—only 16% —of the friction coefficient is recorded when the normal load is multiplied by 10. The dependency of the friction coefficient on the applied normal force is similar to AFM-based friction tests carried out by Bhushan *et al.* on polished silicon, silica, and diamond [37] with nanoscale normal loads. This increase of the friction coefficient with the normal load at the nanoscale is commonly attributed to ploughing. On the other hand, the shape and the and the median value of the frequency distribution is not altered when the scratch speed is increased by 500 %. In the scientific literature, the influence of sliding speed on friction has been linked to the viscoelastic behavior for polymers [38, 39, 40] and rocks [41, 42]. In this case a rate-independent behavior is observed for the friction coefficient showing that for

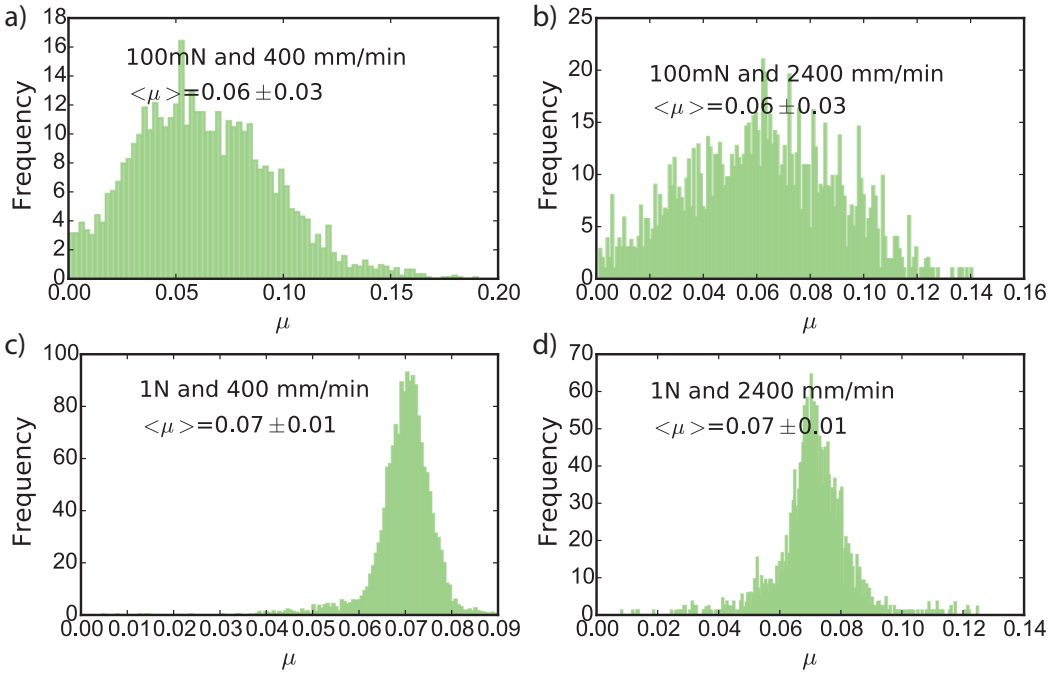

Figure 4: Effect of the normal load and scratch speed on frequency distribution of the friction for aggregate phase. (Color online)

the timescales and length-scales of our experiments, and for the aggregate phase, the visco-elastic energy dissipation is negligible compared to friction-induced energy dissipation. Thus, in what follows, we can consider the friction coefficient to be invariant with respect to the loading rate and scratch speed.

4.3. *Influence of Individual Micro-constituents*

Protocols P4 and P5 were followed to measure the friction and hardness properties of individual micro-constituents: aggregate, silica, hardened cement paste, and rubber. The micro-constituent were selected randomly and tested within specimens from all four mixes Mix 1–4 using optical microscopy. Fig. 5 displays the frequency distribution for both the friction coefficient and the coefficient hardness. For aggregate, silica, and hardened cement paste, the frequency distribution of the friction coefficient exhibits a single peak whereas the frequency distribution of the hardness exhibits several peaks. This difference points to the different nature of hardness—characteristic of strength [30, 43]— and friction. Strength dissipation is due to bulk plastic dissipation taking place inside the probed volume element whereas friction dissipation is due to the interaction of asperities at the surface. As a result, the hardness is primarily influenced by the composition and the morphology whereas friction is primarily driven by the topology of the surfaces in contact. Thus, the different peaks in the hardness frequency distribution is caused by different types of aggregates, silica inclusions, and different cement hydration products.

We can rank the micro-constituents according to the average friction coefficient: in descending order, rubber, cement paste, silica, and aggregate. Friction is promoted in hardened cement paste due to the presence of nanopores, micropores, along with grains boundaries for the cement hydration products. As for silica, its particulate nature–with a particle size ranging from —- promotes asperities at the inclusion boundaries. Finally, rubber presents an intrinsically textured surface. This textured surface, coupled with the bimodal particle distribution—with average 75 μm and 425 μm explain the broad range of the resulting fric-

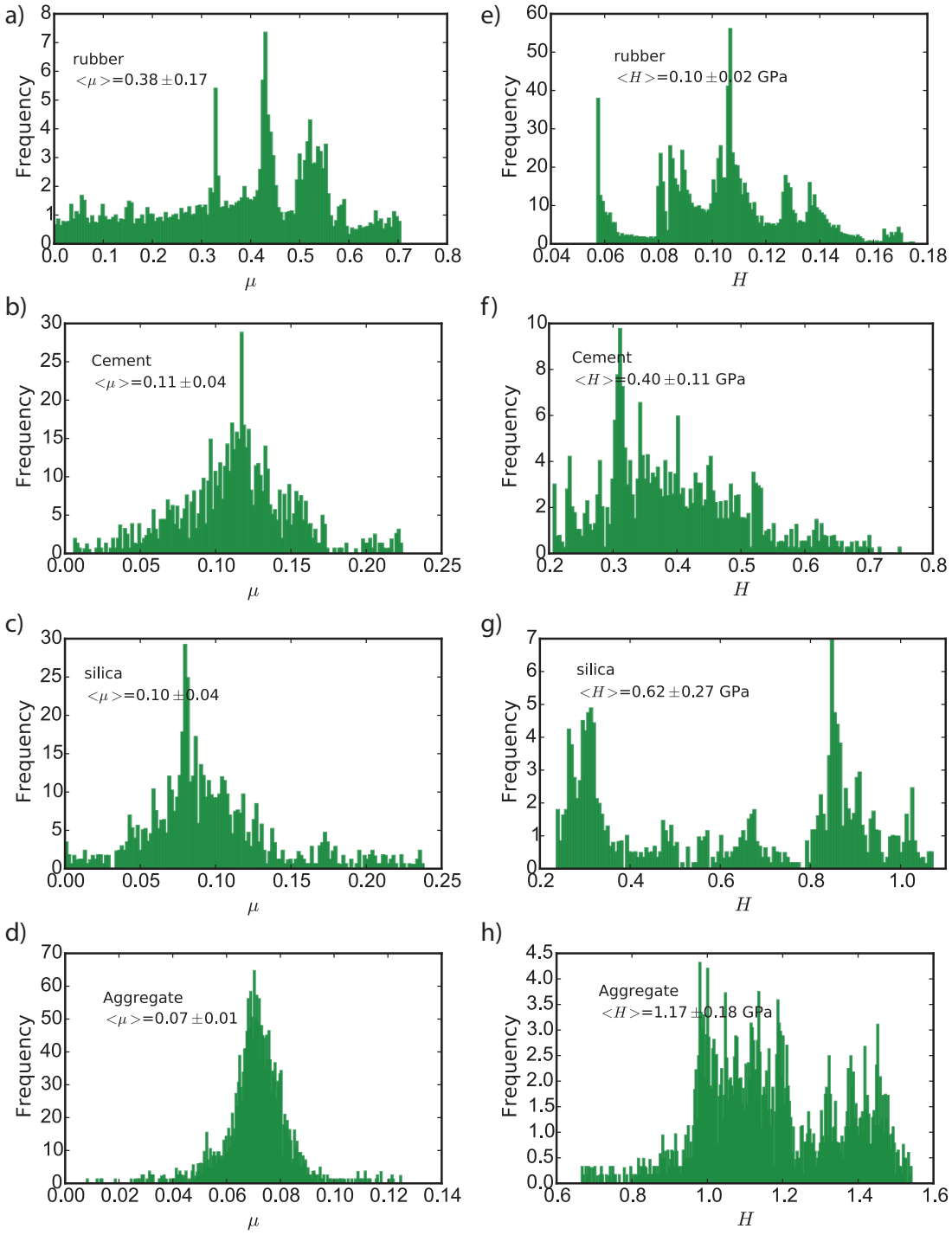

Figure 5: Friction and Hardness of Individual micro-constituents. (Color online)

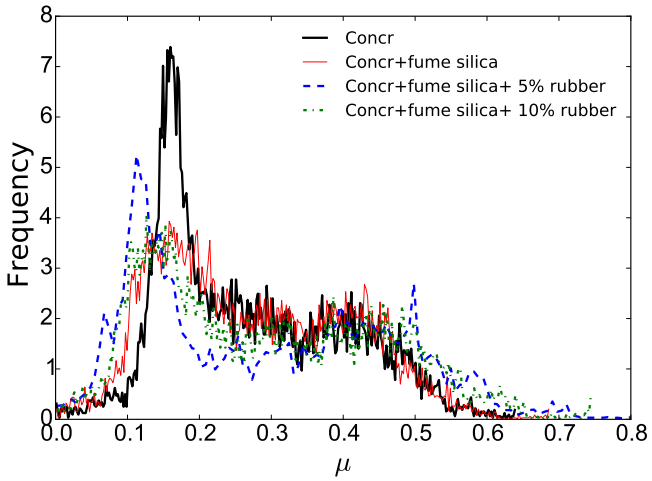

Figure 6: Frequency distribution of the friction coefficient μ for all four mixes, Mix 1–4. (Color online)

tion coefficient. In turn, the micro-constituents can be ranked according to their hardness, in ascending order: rubber, cement paste, silica, and aggregate. The reverse order between friction and hardness suggests a compromise between friction and strength, as characterized by the hardness.

5. Discussion

5.1. Synergistic Effects on Friction

Fig. 6 shows the impact of fume silica and crumb-rubber addition on the friction coefficient. The frequency distribution of the friction coefficient is represented for constant-load scratch tests carried out on materials Mix 1–4 following protocol P1. On the one hand, looking at each curve, separately, we observe a synergistic effect. For instance, Mix 1 exhibits values of the friction coefficient greater than 0.5 whereas its basic constituents—hardened cement paste, silica, and aggregate—are characterized by values of the friction coefficient strictly less than 0.3, cf. Fig. 6 b), c), d). In other words, due to the high heterogeneity and the large local variations in morphology, the effective friction coefficient is significantly higher than that of each microphase considered individually. On the other hand, we note that the frequency distribution is altered by the presence of silica fume and crumbed-rubber. Finally, each frequency distribution curve presents multiple peaks, which are evidence of a discrete range of friction mechanisms.

Table 6 displays the average values of the friction coefficient for constant-load tests under dry conditions for all four mix designs. The friction coefficient μ increases by 1% when fume silica (Mix 2) is added to plain concrete. μ increases by 10% when 75-μm crumb-rubber particles are added at a volume fraction of 5% (Mix 3). Finally, μ increases by 7% when 425-μm crumb-rubber particles are added at a volume fraction of 10% (Mix 4). Although Mix 3 and Mix 4 represent an improvement in terms of friction coefficient with respect to Mix 1 and Mix 2, the increase in the value of the friction coefficient is not proportional to the volume fraction of crumb rubber. The reason is that friction is a surface phenomenon, as a result, the relevant variable is the specific area a of rubber particles. Assuming a statistically uniform dispersion, we have $a \propto \phi_r r^2$ where ϕ_r is the rubber volume content and r is the size of rubber particles. In particular, when comparing Mix 3, and Mix 4, the rubber particles in Mix 3 are in average 5.6 times larger than those in Mix 4; whereas the volume content of Mix 4 is only twice that of Mix 3. Thus, Mix 3 exhibits a specific are which is 15.7 times greater than that of Mix 4, which explains why the increase in friction coefficient is greater for Mix 3 than for Mix 4. Thus, the enhancement in friction coefficient is a function of the specific crumb rubber particle area.

Nevertheless, rubber reinforcement adversely impacts the strength properties. As seen in Table 6, although the average value of the scratch hardness increases by 46% after addition of 10% wt microsilica, a subsequent decrease of 20% and 16% in scratch hardness is recorded after further addition of respectively 5% wt and 10% wt of crumb rubber particles. Similar results have been reported in the literature: a loss in compressive

Property	Mix 1	Mix 2	Mix 3	Mix 4
H, MPa	473.7	690.3	549.08	580.2
μ	0.270	0.273	0.297	0.289
K_c, MPa $\sqrt{m}$	0.34	0.44	0.47	0.38
η	0.40	0.51	0.54	0.42
β	2.15	4.04	2.42	3.18

Table 6: Influence of crumb rubber content and fume silica content on aggregate mechanical characteristics. H is the scratch hardness, μ is the friction coefficient, and K_c is the fracture toughness. Moreover η and β are the Weibull scale and shape distribution parameters.

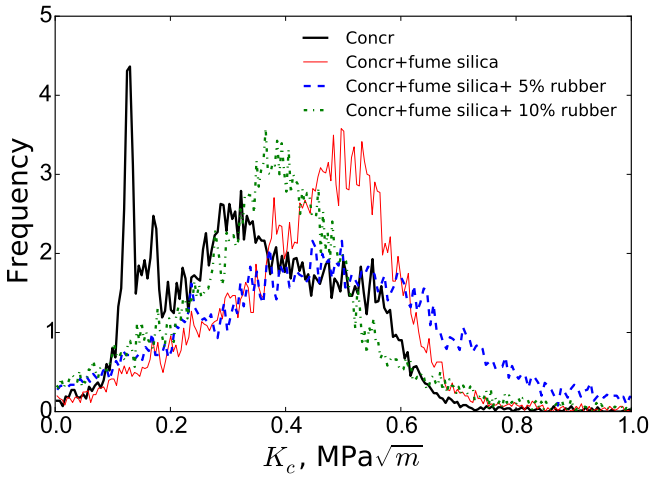

Figure 7: Frequency distribution of the fracture toughness K_c for all four materials. (Color online)

strength was observed after partial replacement of aggregates by crumb rubber in self-compacting concrete [14, 44]. Furthermore, the strength loss was positively correlated to the volume content of rubber [44]. However, in our case, due to imperfect bonding between the rubber particles and the surrounding hardened cement matrix, additional air voids where incorporated in the mix as seen in Fig. 1 b). This increase in porosity $\Delta\phi$ due to improper bonding is proportional to the rubber particle size r and the rubber volume content ϕ_r: $\Delta\phi \propto 2\pi r t \phi_r$, where t is the thickness of rubber particles. As a result, the relative increase in porosity due to improper bonding is 2.5 times greater for Mix 3 than for Mix 4. Therefore, the additional porosity due to improper bonding explains the slightly lower scratch hardness of Mix 3 compared to Mix 4. Nevertheless, the joint addition of fume silica and crumb-rubber results in an overall increase in scratch hardness of more than 15 % compared to the reference mix, plain concrete (Mix 1).

5.2. Mesoscale Fracture Behavior

Fig. 7 displays the frequency distribution of the fracture toughness for all specimens. The scratch-based fracture tests were carried out following protocol P 4, and the results were analyzed using Eq. (4). In addition, for each specimen the frequency distribution was evaluated based on the population consisting of all measurements for all scratch tests performed. A two-parameter Weibull distribution was adopted to fit the frequency distribution function of the fracture toughness K_c according to:

$$f(x) = \frac{\beta}{\eta}\left(\frac{x}{\eta}\right)^{\beta-1} \exp\left(-\left(\frac{x}{\eta}\right)^{\beta}\right) \quad (5)$$

where f is the probability distribution function of the variable $x \equiv K_c$, η is the scale parameter and β is the shape parameter. Table 6 lists the values of the scale and shape parameters, η and β, as well as the average value of the fracture toughness K_c. Both the scale parameter η and the shape parameter vary for different mix design: in other words, the mix design influences the frequency distribution of the fracture resistance. The addition of fume silica and crumb-rubber contributes to shifting the frequency distribution curve towards high values.

The average fracture toughness K_c increases by 29% by addition of microsilica, and by 38% and 12% after subsequent addition of respectively 5% and 10% crumb rubber. Our findings concur with that of other scientists who reported an en-

hancement in fracture resistance after addition of crumb rubber particles [12]. The gain in fracture resistance is commonly attributed to the intrinsic ductility of rubber particles as well the presence of toughening mechanisms such as crack ligament bridging, which are promoted by the presence of rubber particles.

5.3. Influence of Surface Lubricant or Resistance to Weathering

In railway applications, a major concern is to appraise the durability of materials in harsh environmental conditions: wet due to water (rain, snow) or oil (leaking from an engine). Thus, we assessed the the influence of lubricant on the surface properties via surface lubrication with oil and deionized water as per protocols P 2–3. Fig. 8 displays the distribution of the friction coefficient for all four mixes and for all three surface conditions: dry, wet with oil, and wet with water. In addition, cluster analysis was implemented to decompose the overall probability distribution of the friction coefficient as a weighted sum of individual Gaussian distributions [45, 46]. Herein, each single Gaussian distribution represents a specific friction micromechanism. Friction is a surface phenomena that results from the interlocking of surface asperities. A the microscopic and nanoscale, friction depends on a wide range of parameters such as asperity density, asperity radius of curvature, contact shear strength, contact junction plastic yield strength, etc. [47]. We opt for a discrete representation of this continuum of friction-inducing micromechanisms using cluster analysis and multivariate mixture analysis [45, 46]. Section 7 in the Appendix displays the weights and average friction coefficient of each individual micromechanisms, whereas the corresponding probability distribution curves are shown in Fig. 8.

Without crumb rubber, high-net-friction micromechanisms are curbed due to chemical reactivity. For instance, for the reference specimen, Mix 1 without crumb rubber, friction micromechanisms with a net average friction coefficient of 0.45 and above are drastically suppressed after surface wetting with oil or deionized water. This drastic reduction in high-net-friction mechanisms is even more noticeable for surface treatment with deionized water. A plausible reason is the interaction of water molecules with hardened cement paste. Surface water may activate a further hydration of cement paste, seep into the cement paste micropores and nanopores, locally increase the pore pressure and generate additional microcracking. As a result of the interaction between cement paste and water, local topological features such as asperities may be masked, resulting in a smoothing of the surface. A similar phenomenon is observed for Mix 2 (conc+silica) when the surface is wet with water. In this case, the water will contribute to sub-critical cracking of silica via stress corrosion cracking [48].

In contrast, crumb rubber inclusions promote the rise of high-net-friction micromechanisms. For Mix 3 (conc+silica+5% wt rubber), friction micromechanisms with a net average friction coefficient greater than 0.5 are still active in presence of oil or water. As a result, for Mix 3, higher values of the friction coefficient were recorded in presence of water and oil. One reason is the chemical inertia of rubber with respect to water and oil which contributes to an enhancement of local asperities. Mix 4 (conc+silica+10% wt rubber) experiences a sharper decrease of the friction coefficient when the surface is treated with oil. This might be due to the smaller specific surface are R_a of the crumb rubber. nevertheless, overall the partial replacement of aggregates with crumb rubber contributes to a higher resistance to weathering and an improved stability of surface friction properties with respect to surface treatment with a lubricant.

6. Conclusions

To understand the tribological behavior of crumb-rubber concrete, scratch testing has been applied at different length-scales,

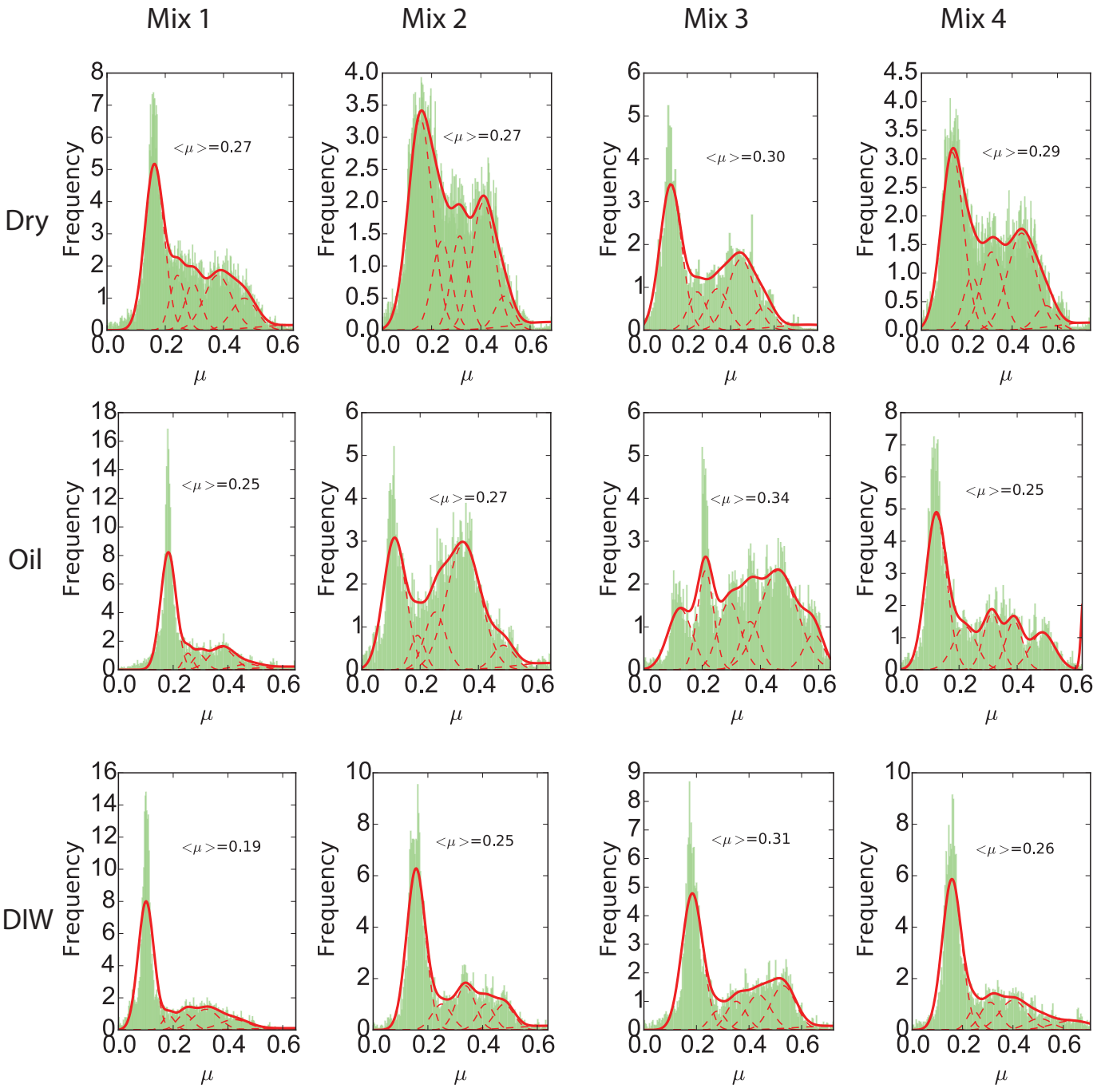

Figure 8: Influence of lubricant on friction coefficient. (Color online)

and under different loading and speed rates, and for various surface treatments. Optical microscopy and scanning electron microscopy were utilized to identify the micro-constituents, whereas contact mechanics and fracture mechanics were utilized to yield the mechanical characteristics. Based on the testing results, the following conclusions can be derived:

1. Crumb rubber inclusions contribute to an increase in the effective friction behavior.
2. An enhancement of the fracture toughness is observed with the addition of crumb rubber particles.
3. A high resistance to weathering a higher stability in the tribological response with respect to surface lubrication is observed for crumb-rubber reinforced concrete.
4. The specific surface area of crumb rubber particles may plan a crucial roles in governing the level on improvement of the friction coefficient. In addition, the functionalization of the cement/rubber interface using bonding agent may stall the decrease in strength observed due to the partial replacement of aggregates with crumb rubber particles. Nevertheless, further research is needed.

Thus, these results will contribute to the development of enhanced-performance materials for railroad applications.

Acknowledgments

The research was funded by the Birmingham-Illinois Partnership for Discovery, Engagement and Education (BRIDGE). The research was also funded by the Start-Up funds of Prof. Akono that were provided jointly by the Department of Civil and Environmental Engineering as well as the College of Engineering at the University of Illinois at Urbana-Champaign. We are thankful to Caroline V. Johnson for the help in carrying out part of scratch friction tests. This research was carried out in part in the Frederick Seitz Materials Research Laboratory Central Research Facilities, University of Illinois, and was also partly carried out in part in the Imaging Technology Group at the Beckman Institute for Advanced Science and Technology at the University of Illinois.

References

[1] Raffoul, S. and Garcia, R. and Pilakoutas, K. and Guadagnini, M. and Medina, N.-F., Optimization of rubberized concrete with high rubber content: An experimental investigation, Construction and Building Materials, (2016), Vol. 124, pp. 391–404, DOI: 10.3390/ma9030172.

[2] Liu, H. and Wang, X. and Jiao, Y. and Sha, T., Experimental investigation of the mechanical and durability properties of crumb rubber concrete, Materials, (2016), Vol. 9, DOI: 10.3390/ma9030172.

[3] Skariah Thomas, B. and Chandra Gupta, R. and Panicker, V.-J., Recycling of waste tire rubber as aggregate in concrete: durability-related performance, Journal of Cleaner Production, (2016), Vol. 112, pp. 504–513.

[4] Shu, X. and Huang, B., Recycling of waste tire rubber in asphalt and Portland cement concrete: An overview, Construction and Building Materials, (2014), Vol. 67, pp. 217–224.

[5] Sukontasukkul, P. and Chaikaew, C., Properties of concrete pedestrian block mixed with crumb rubber, Construction and Building Materials, (2006), Vol. 20, pp. 450–457, DOI: 10.1016/j.conbuildmat.2005.01.040.

[6] Kaewunruen, S. and Remennikov, A. M., Sensitivity analysis of free vibration characteristics of an in situ railway concrete sleeper to variations of rail pad parameters, Journal of Sound and Vibration, (2006), Vol. 298, pp. 453–461, DOI: 10.1016/j.jsv.2006.05.034.

[7] Kaewunruen, S. and Remennikov, A. M., Experiments into impact behavior of railway prestressed concrete sleepers, Engineering Failure Analysis, (2011), Vol. 18, pp. 2305–2315, DOI: 10.1016/j.engfailanal.2011.08.007.

[8] Mull, M. A. and Stuart, K. and Yehia, A., Fracture resistance characterization of chemically modified crumb rubber asphalt pavement, Journal of Materials Science, (2002), Vol. 37, pp. 557–566.

[9] Xi, Y. and Li, Y.and Xie, Z. and Lee, J. S., Utilization of solid wastes (waste glass and rubber particles) as aggregates in concrete, Workshop on Sustainable Development and Concrete Technology, (2004), pp. 45–54.

[10] Gupta, T. and Chaudhary, S. and Sharma, R.-K., Assessment of mechanical and durability properties of concrete containing waste rubber tire as fine aggregate, Construction and Building Materials, (2014), Vol. 73, pp. 562–574, DOI: 10.1016/j.conbuildmat.2014.09.102.

[11] Atahan, A. O. and ner Ycel, A., Crumb rubber in concrete: Static and

dynamic evaluation, Construction and Building Materials, (2012), Vol. 36, pp. 617–622.

[12] M. M. Reda Taha, A. S. El-Dieb, M. A. Abd El-Wahab, M. E. Abdel-Hameed, Mechanical, Fracture, and Microstructural Investigations of Rubber Concrete, Journal of Materials in Civil Engineering, (2008), Vol. 10, pp. 640–649, DOI: 10.1061/(ASCE)0899-1561(2008)20:10(640).

[13] N. Ganesan, J. Bharati Raj, A.P. Shashikala, Flexural fatigue behavior of self compacting rubberized concrete, Construction and Building Materials, (2013), Vol. 44, pp. 7–14, DOI: 10.1016/j.conbuildmat.2013.02.077.

[14] N. Ganesan, Bharati Raj. J and A.P. Shashikala, Strength and durability studies of self compacting rubberised concrete, The Indian Concrete Journal, (2012), pp. 15–23.

[15] R. W. Carpick, Scratching the Surface: Fundamental Investigations of Tribology with Atomic Force Microscopy, Chemical Reviews, (1997), Vol. 97, pp. 1163–1194.

[16] M. A. Lantz, S. J. O'Shea, A. C. F. Hoole, M. E. Welland, Lateral stiffness of the tip and tip-sample contact in frictional force microscopy, Applied Physics Letters, (1997), Vol. 70, pp. 970.

[17] Alva Peled, Jason Weiss, Hydrated cement paste constituents observed with Atomic Force and Lateral Force Microscopy, Construction and Building Materials, (2011), Vol. 25, pp. 4299–4302, DOI: 10.1016/j.conbuildmat.2011.04.066.

[18] A. Peled, J. Castro, W.J. Weiss, Atomic force and lateral force microscopy (AFM and LFM) examinations of cement and cement hydration products, Cement and Concrete Composites, (2013), Vol. 36, pp. 48–55, DOI: 10.1016/j.cemconcomp.2012.08.021.

[19] M. Jafarbeglou, M. Abdouss, A. A. Ramezanianpour, Nanoscience and Nano Engineering in Concrete Advances A Review, Int. J. Nanosci. Nanotechnol., (2015), Vol. 11, pp. 263–273.

[20] Bull, S. J., Can scratch testing be used as a model for the abrasive wear of hard coatings, Wear, (1999), Vol. 233–235, pp. 412–423.

[21] Jardret, V. and Zahouani, H. and Loubet, J.-L. and Mathia, T.-G., Understanding and quantification of elastic and plastic deformation during a scratch test, Wear, (1998), Vol. 218, pp. 8–14.

[22] Li, K. and Shapiro, Y. and Li, J.-C.-M., Scratch test of soda-lime glass, Acta Materialia, (1998), Vol. 46, pp. 5569–5578.

[23] Liang, Y.N. and Li, S.-Z. and Li, D.-F. and Li S., Some developments for single-pass pendulum scratching, Wear, (1996), Vol. 199, pp. 66–73.

[24] Low, S. R. , Rockwell Hardness of Metallic Materials, National Institute of Standards and Technology, Special Publication, (2001), DOI: 10.1016/0003-4916(63)90068-X.

[25] Subhash, G. and Zhang, W., Investigation of the overall friction coefficient in single-pass scratch test, Wear, (2002), Vol. 252, pp.123–134.

[26] Miller, M. and Bobko, C. and Vandamme, M. and Ulm, F.-J., Surface roughness criteria for cement paste nanoindentation, Cement and Concrete Research, (2008), Vol. 38, pp. 467–476.

[27] Xu, J. and Yao, W., Nano-scratch as a new tool for assessing the nano-tribological behavior of cement composite, Materials and Structures, (2011), Vol. 44, pp. 1703–1711, DOI:110.1617/s11527-011-9728-7.

[28] Anton Paar Specification, (2016).

[29] ASTM, ASTM G171-03: Standard test method for scratch hardness of materials using a diamond stylus1, ASTM International, West Conshohocken, PA (2009), DOI:10.1520/G0171-03.

[30] J.A. Williams, Analytical models of scratch hardness, Tribology International, (1996), Vol. 29, pp. 675–694.

[31] Ange-Therese Akono, Nicholas X. Randall, Franz-Josef Ulm, Experimental determination of the fracture toughness via microscratch tests: Application to polymers, ceramics and metals, Mat. Res. Soc., 27, (2012), 485-493

[32] Akono, A.-T. and Ulm, F.-J., An improved technique for characterizing the fracture toughness via scratch test experiments, Wear, (2014), Vol. 313, pp. 117–124.

[33] Akono, A.-T., Energetic Size Effect Law at the Microscopic Scale: Application to Progressive-load Scratch Testing, ASCE's Journal of Nanomechanics and Micromechanics, (2015), DOI: 10.1061/(ASCE)NM.2153-5477.0000105.

[34] Anderson, K. and Akono, A.T., 2017. Microstructuretoughness relationships in calcium aluminate cementpolymer composites using instrumented scratch testing. Journal of Materials Science, 52(22), pp.13120-13132.

[35] Akono, A.T., Reis, P.M. and Ulm, F.J., 2011. Scratching as a fracture process: From butter to steel. Physical review letters, 106(20), p.204302.

[36] Akono, A.T. and Kabir, P., 2016. Microscopic fracture characterization of gas shale via scratch testing. Mechanics Research Communications, 78, pp.86-92.

[37] Bhushan, B. and Kulkarni, A.V., Effect of normal load on microscale friction measurements, Thin Solid Films, (1996), Vol. 278, pp. 49–56, DOI: 10.1016/0040-6090(95)08138-0.

[38] Roth, F.-L. and Driscoll, R.-L. and Holt, W.-L., Frictional Properties of Rubber, Rubber Chemistry and Technology, (1943), Vol. 16, pp. 155–177, DOI:10.5254/1.3540095.

[39] Mclaren, K.-G. and Tabor, D., Visco-Elastic Properties and the Friction of Solids: Friction of Polymers: Influence of Speed and Temperature, Nature, (1963), Vol. 197, pp. 856–858, DOI: 10.1038/197856a0.

[40] Bouissou, S. and Petit, J.-P. and Barquins, M, Normal load, slip rate and roughness influence on the polymethylmethacrylate dynamics of sliding

1.Stable sliding to stick-slip transition, Wear, (1998), Vol. 214, pp.156–164.

[41] Ruina A., Slip instability and state variable friction laws, Journal of Geophysical Research, (1983), DOI: 10.1029/JB088iB12p10359.

[42] Dieterich J. H., Kilgore B. D., Direct observation of frictional contacts: New insights for state-dependent properties, Pure and Applied Geophysics, (1994), Vol. 143, pp. 283–302.

[43] Romain Bard, Franz-Josef Ulm, Scratch hardnessstrength solutions for cohesive-frictional materials, Journal for Numerical and Analytical Methods in Geomechanics, (2012), Vol. 36, pp. 307–326, DOI: 10.1002/nag.1008.

[44] Raj, B., Ganesan, N. and Shashikala, A.P., 2011. Engineering properties of self-compacting rubberized concrete. Journal of Reinforced Plastics and Composites, 30(23), pp.1923-1930.

[45] McLachlan, G. and Peel, D., 2004. Finite mixture models. John Wiley & Sons.

[46] Fraley, C. and Raftery, A.E., 1998. How many clusters? Which clustering method? Answers via model-based cluster analysis. The computer journal, 41(8), pp.578–588.

[47] Boitnott, G.N., Biegel, R.L., Scholz, C.H., Yoshioka, N. and Wang, W., 1992. Micromechanics of rock friction 2: Quantitative modeling of initial friction with contact theory. Journal of Geophysical Research: Solid Earth, 97(B6), pp.8965–8978.

[48] Atkinson, B.K., 1979. A fracture mechanics study of subcritical tensile cracking of quartz in wet environments. Pure and Applied Geophysics, 117(5), pp.1011–1024.

Appendix

7. Mixture Analysis of Friction Frequency Distribution: Effect of Surface Lubricant

Tables 7–10 below display the characteristics of the individual friction mechanisms identified for each mix and for each surface treatment condition. Three surface treatment were considered; Dry, wet witl Oil and wet with Deionized Water. The individual friction mechanisms are characterized by their fraction, (%), average friction coefficient, $< \mu >$, and standard deviation of the friction coefficient, $< \sigma_\mu >$.

Mix 1		Mechanism 1	Mechanism 2	Mechanism 3	Mechanism 4	Mechanism 5	Mechanism 6
	(%)	0.43	0.11	0.10	0.20	0.11	0.05
Dry	$< \mu >$	0.16	0.24	0.30	0.38	0.47	0.64
	σ_μ	0.03	0.03	0.03	0.05	0.04	0.13
	(%)	0.59	0.05	0.07	0.18	0.05	0.07
Oil	$< \mu >$	0.18	0.25	0.30	0.38	0.47	0.65
	σ_μ	0.03	0.02	0.02	0.05	0.05	0.12
	(%)	0.58	0.05	0.07	0.15	0.09	0.05
DI Water	$< \mu >$	0.10	0.18	0.24	0.32	0.42	0.65
	σ_μ	0.03	0.02	0.03	0.05	0.05	0.17

Table 7: Deconvolution analysis of the friction distribution for Mix 1.

Mix 2		Mechanism 1	Mechanism 2	Mechanism 3	Mechanism 4	Mechanism 5	Mechanism 6
	(%)	0.41	0.13	0.13	0.23	0.05	0.05
Dry	$< \mu >$	0.15	0.24	0.31	0.41	0.49	0.69
	σ_μ	0.05	0.04	0.03	0.05	0.04	0.15
	(%)	0.30	0.05	0.12	0.43	0.05	0.05
Oil	$< \mu >$	0.11	0.19	0.25	0.35	0.49	0.65
	σ_μ	0.04	0.02	0.04	0.06	0.04	0.12
	(%)	0.54	0.09	0.15	0.08	0.09	0.05
DI Water	$< \mu >$	0.16	0.25	0.34	0.41	0.48	0.64
	σ_μ	0.03	0.04	0.04	0.03	0.04	0.12

Table 8: Deconvolution analysis of the friction distribution for Mix 2.

Mix 3		Mechanism 1	Mechanism 2	Mechanism 3	Mechanism 4	Mechanism 5	Mechanism 65
	(%)	0.45	0.07	0.12	0.18	0.10	0.07
Dry	$< \mu >$	0.12	0.23	0.31	0.41	0.49	0.57
	σ_μ	0.05	0.03	0.04	0.04	0.03	0.04
	(%)	0.15	0.16	0.15	0.09	0.37	0.07
Oil	$< \mu >$	0.12	0.21	0.29	0.36	0.46	0.58
	σ_μ	0.04	0.03	0.04	0.03	0.06	0.03
	(%)	0.48	0.05	0.09	0.14	0.18	0.05
DI Water	$< \mu >$	0.18	0.28	0.35	0.44	0.53	0.72
	σ_μ	0.04	0.03	0.04	0.05	0.05	0.14

Table 9: Deconvolution analysis of the friction distribution for Mix 3.

Mix 4		Mechanism 1	Mechanism 2	Mechanism 3	Mechanism 4	Mechanism 5	Mechanism 6
	(%)	0.38	0.09	0.16	0.26	0.05	0.05
Dry	$< \mu >$	0.14	0.22	0.31	0.44	0.55	0.75
	σ_μ	0.05	0.04	0.05	0.06	0.05	0.15
	(%)	0.43	0.14	0.13	0.11	0.12	0.06
Oil	$< \mu >$	0.12	0.22	0.31	0.39	0.49	0.63
	σ_μ	0.04	0.04	0.03	0.03	0.04	0.01
	(%)r	0.56	0.05	0.10	0.16	0.06	0.07
DI Water	$< \mu >$	0.16	0.24	0.31	0.40	0.51	0.64
	σ_μ	0.04	0.03	0.04	0.05	0.05	0.08

Table 10: Deconvolution analysis of the friction distribution for Mix 4.